Check for updates

Co-adsorption of an anionic dye in the presence of a cationic dye and a heavy metal ion by graphene oxide and photoreduced graphene oxide†

Xiaorong Zhang,[ab] Chengbing Qin, [ID] *[ab] Yani Gong,[ab] Yunrui Song,[ab] Guofeng Zhang,[ab] Ruiyun Chen,[ab] Yan Gao,[ab] Liantuan Xiao*[ab] and Suotang Jia[ab]

To investigate the adsorption behavior of contaminants with different adsorbents and co-adsorbates under identical conditions, the adsorption capacities of anionic orange II (OII) dye onto graphene oxide (GO) and photoreduced GO (PRGO) in a single-component system and in the presence of cationic methylene blue (MB) dye as well as heavy metal ion Pb^{2+} were explored. In this work, PRGO was prepared by solar light irradiation of a GO dispersion. GO and PRGO were characterized by Fourier transform infrared spectroscopy, X-ray photoelectron spectroscopy, X-ray diffraction, Raman spectroscopy, atomic force microscopy, scanning electron microscopy, and transmission electron microscopy. The adsorption isotherms of OII, MB, and Pb^{2+} onto GO and PRGO in single and binary systems have been studied and analyzed by the Langmuir model. In the single system, the adsorption capacity of OII on GO can be promoted from 8.4 mg g^{-1} to 32.5 mg g^{-1} after solar light irradiation. While the adsorption capacities of MB and Pb^{2+} are not affected by the photoreduction process. In the binary system, a marked synergistic effect for the adsorption of OII has been determined in the presence of both MB and Pb^{2+}, where the adsorption capacity of OII on PRGO has been improved from 8.4 mg g^{-1} to 295 mg g^{-1} and 105 mg g^{-1}, enhancements of 35- and 12.5-fold, respectively. In contrast, the presence of OII leads to a mildly antagonistic effect on the adsorption of MB and Pb^{2+}. These findings show that the adsorption of anionic dyes by graphene-based materials can be strongly improved in the presence of either cationic dyes or heavy metal ions, which will be of great value in practical applications.

1. Introduction

The shortage of fresh and clean water has become one of the most important challenges around the world, with serious water pollution arising from the rapid development of industry endangering human health.[1,2] Among water pollutants, organic dyes and heavy metal ions have attracted great attention because they are non-biodegradable and tend to accumulate in living organisms.[3] Various technologies have been developed for the removal of these dyes and metal ions from wastewater,

aState Key Laboratory of Quantum Optics and Quantum Optics Devices, Institute of Laser Spectroscopy, Shanxi University, Taiyuan, Shanxi 030006, China. E-mail: chbqin@sxu.edu.cn; xlt@sxu.edu.cn

bCollaborative Innovation Center of Extreme Optics, Shanxi University, Taiyuan, Shanxi 030006, China

† Electronic supplementary information (ESI) available: Batch adsorption experiments in single-component and binary systems, absorption spectra of OII and MB in single-component solute as well as that of OII/MB in binary solute, BET measurements of GO and PRGO, Freundlich and Temkin model simulations for OII, MB, and Pb^{2+} in single-component system and corresponding fitted parameters, Langmuir model simulation for MB/OII, OII/MB, OII/Pb^{2+}, and Pb^{2+}/OII binary systems and corresponding fitted parameters. See DOI: 10.1039/c8ra09438a

including membrane separation,[4] ion exchange,[5] chemical precipitation[6] and adsorption. Of all these technologies proposed, adsorption is considered as a globally acclaimed water treatment process due to its versatility, economic feasibility and wide applicability.[3] In the last 70 years,[7] many adsorbents have been investigated, such as activated carbon,[8,9] magnetic carbon,[10,11] chitosan,[12,13] clay,[14] ethyl cellulose[15] and so on.

As newly developed types of carbon materials, very recently graphene and its derivatives have been considered as effective adsorbents, due to their unique physical and chemical properties, such as superior mechanical flexibility, ultrahigh specific surface area, and abundant surface functionality with oxygen-containing functional groups.[16–18] The adsorption behaviors of graphene-based materials, such as graphene oxide (GO) and reduced graphene oxide (RGO), for different contaminants have been studied, where they usually showed outstanding adsorption capacities. For example, the adsorption capacity of poly-pyrrole–RGO hybrid material for Hg^{2+} has been reported to reach 980 mg g^{-1}.[19] Obtained by *in situ* reduction of GO with sodium hydrosulfite, RGO provides a maximum adsorption capacity of 3300 mg g^{-1} for acridine orange dye.[20] In particular, graphene-based materials are now available commercially in

high production volume.[21,22] These materials exhibited comparable or better adsorption capacities than commercial activated carbon in some conditions.[23–26] Consequently, they can serve as alternative adsorbents for removing contaminants from sewage water. However, so far the investigations of adsorption behaviors of contaminants by graphene-based materials have generally been performed in single-component systems.[27,28] While in practical applications of wastewater treatment, several kinds of contaminants often coexist as pollutants. In such cases, investigating the co-adsorption behaviors of adsorbents for coexisting contaminants is of vital importance for selecting and utilizing these graphene-based materials.

To our knowledge, only a few works have been focused on the co-adsorption of dyes and heavy metal ions[29–31] by GO and its hybrid materials, where the adsorption behaviors and mechanisms are still controversial. Xiao and coworkers have reported that the presence of anionic indigo carmine lowered the removal ability of cationic neutral red by L-cysteine-reduced graphene oxide (CRG),[32] while there emerged a remarkable synergistic effect when adsorbing onto CRG/poly(vinyl alcohol) aerogel.[33] For metal ion-dye binary systems, the adsorption behaviors are more noteworthy. Deng *et al.* found that the adsorption capacity of Cd^{2+} onto magnetic GO was suppressed with increasing methylene blue (MB) initial concentration.[34] While Liu and coworkers reported that the presence of MB in water promoted the adsorption of Pb^{2+} on montmorillonite-pillared GO.[35] Furthermore, the Kang group determined that the adsorption capacity of Cr^{6+} onto magnetite (Fe_3O_4)/non-oxidative graphene was not affected by increasing of MB concentration.[36] That is, for different adsorbents or co-adsorbates, the presence of MB may lead to completely different effects. Therefore, it is necessary to investigate the adsorption behaviors of contaminants with different adsorbents and co-adsorbates under identical conditions to compare their capacities. These results will be of vital importance for the optimization of adsorption capacities and practical applications.

In this work, we employed commercial GO and photo-reduced GO (PRGO) as the adsorbents to evaluate the adsorption of dyes and metal ions in single and binary systems by batch experiments. The anionic dye orange II (OII) and cationic dye MB, and Pb^{2+} were chosen as model dyes and heavy metal ion, respectively, owing to their wide use in leather dyeing and battery manufacturing processes. An environmentally friendly and cost-free method was used to produce PRGO, which was prepared by exposing GO dispersion to solar light irradiation in sealed glasses with different duration times. GO and PRGO were characterized by Fourier transform infrared (FTIR) spectroscopy, Raman spectroscopy, X-ray diffraction (XRD), X-ray photoelectron spectroscopy (XPS), atomic force microscopy (AFM), scanning electron microscopy (SEM), and transmission electron microscopy (TEM). The adsorption isotherms of GO and PRGO for OII, MB, and Pb^{2+} in single-component systems, as well as in OII-MB and OII-Pb^{2+} binary systems have been investigated. The results revealed that the adsorption capacities of OII are remarkably enhanced in the presence of MB and Pb^{2+}, while those of MB and Pb^{2+} are suppressed in the presence of OII. Also, the main adsorption mechanism through relevant models has been discussed.

2. Materials and methods

2.1 Materials

GO powder (diameter of 0.5–5 μm and thickness of 1–3 nm) was supplied by Nanjing XFNANO Materials Tech Co. Ltd. OII, MB and lead nitrate $(Pb(NO_3)_2)$ were purchased from J&K Scientific Ltd. 0.22 μm Millipore syringe filters were obtained from Tianjin Navigator Lab Instrument Co. Ltd. An Elix® Advantage system (Millipore Q, USA) was used to produce deionized water. All regents were used without further purification.

2.2 Preparation of PRGO

In our previous work,[37] we presented an environmentally friendly and cost-free method to prepare PRGO dispersion. The reduction of GO was carried out by exposing 0.67 mg mL^{-1} dispersion to solar light with duration times of each of 24, 48, and 72 hours. In order to maintain the same reduction conditions, the experiments were performed at the same weather temperature (generally from 10 a.m. to 4 p.m. between June and September) and atmospheric environment (cloudless). Initial pH value of the dispersion was measured to be 5.0 ± 0.3 and no significant change was observed after photoreduction. The PRGO obtained with these three irradiation durations are named hereinafter as PRGO-1, PRGO-2, and PRGO-3, respectively.

2.3 Sample characterizations

The concentrations of dyes were determined using a UV-visible spectrometer (Ocean Optics May2000Pro). The chemical structure and elemental composition of GO and PRGO were characterized by means of FTIR and Raman spectroscopies, XRD, and XPS. FTIR spectra were recorded on a Si substrate with a commercial Bruker FTIR spectrometer (Thermo Scientific Nicolet iS50). Raman spectra were obtained with a home-built scanning confocal system, the details of which can be found in our previous works.[37,38] XRD measurements were performed by use of a Rigaku BD 2000 system with Cu Kα X-rays (0.154 nm) operating at 30 kV and 20 mA. XPS analysis was conducted using an AXIS ULTRA DLD spectrometer (Thermo Kratos British) with Al Kα irradiation as the exciting source (300 W). AFM (5000N, JEOL) was used to measure the height of GO and PRGO. The surface morphology of nanomaterials was observed using SEM (SU8010, Hitachi) and TEM (Philips model CM10).

2.4 Batch adsorption experiments

2.4.1 Single-component adsorption experiments. Adsorption capacities of GO and PRGO in single and binary systems were determined by mixing 2 mg GO or PRGO with a series of contaminant (OII, MB, Pb^{2+}) solutions at different initial concentrations (C_0) at room temperature (25 °C) in sealed glass bottles. After shaking at 80 rpm in a shaker, the suspensions were withdrawn and filtered with 0.22 μm Millipore syringe filters. The residual concentrations (C_e) of dyes were calculated

according to UV-visible absorption spectra based on their maximum absorption wavelengths at 510 and 665 nm for OII and MB, respectively (the absorption spectra of OII and MB in single and binary systems are presented in Fig. S1–S3 in the ESI†). Calibration plots of dye concentrations were established based on the Lambert–Beer law. The concentration of Pb^{2+} was measured by a lead ion meter (Bante931-Pb, Benchtop, China). The amount of contaminants adsorbed at equilibrium q_e (mg g^{-1}) can be obtained by the equation:

$$q_e = \frac{(C_0 - C_e) \times V}{m} \tag{1}$$

where V is the volume of the solution (L) and m is the mass of GO or PRGO (g). The detailed parameters used in single systems can be found in Section 1 of ESI.†

2.4.2 Co-adsorption isotherms in binary systems. For co-adsorption in binary systems, we mainly focus on the synergistic or competitive effect between two contaminants. The investigations were conducted in the form of A/B, representing the maximum adsorption capacity of contaminant A influenced by the presence of contaminant B with a constant concentration. Generally, in the experiments, the concentration of contaminant A was varied to obtain the maximum adsorption capacity based on isotherm models. Taking OII/MB as an example, the concentration of MB was firstly fixed at 100 mg L^{-1}, and the concentration of OII was varied from 66.7 mg L^{-1} to 100, 133.3, 166.7, 200, 233.3, 266.7 and 300 mg L^{-1}. In this case, the volume of mixed solution was 3 mL, and the mass of GO or PRGO was 2 mg. After shaking for 24 hours, the residual concentrations of OII were calculated by absorption spectroscopy. Then, the concentration of MB was

increased to 200 mg L^{-1} or 300 mg L^{-1}, while the concentration of OII was still varied from 66.7 mg L^{-1} to 300 mg L^{-1}. Consequently, the maximum adsorption capacities of OII influenced by MB with concentrations of 100, 200, and 300 mg L^{-1} will be determined. The detailed parameters used in binary systems can be found in Section 2 of ESI.†

3.   Results and discussion

3.1   Characterizations of GO and PRGO

The chemical components of GO before and after solar light irradiation were investigated by FTIR and Raman spectroscopies and XRD. Fig. 1a presents the FTIR spectra of GO and PRGO with irradiation duration of 72 hours. For original GO, the strong and broad band centered at 3398 cm^{-1} is attributed to the vibration mode of O–H bond (hydroxyl). The peaks at 1733, 1623, and 1069 cm^{-1} correspond to the stretching vibrations of C=O (carbonyl and carboxyl), C=C, and C–O (alkoxy) bonds, respectively. The bands at 1409 cm^{-1} and 1323 cm^{-1} are assigned to the bending vibration of C–OH group as well as C–O–C asymmetric stretching vibration of epoxy group. The presence of these functional groups is consistent with previous reports.[37,39] For PRGO, the intensities of bands corresponding to O–H, C=O, and C=C bonds are much weaker compared with those of GO, and the other bands are even absent. These results indicate that many oxygen-containing functional groups are successfully removed *via* solar light irradiation. Fig. 1b displays the Raman spectra of GO and PRGO. Two prominent peaks can be clearly determined, which correspond to D and G bands, respectively. No obvious shifts of the two bands before and after solar light irradiation are determined; however, the increased
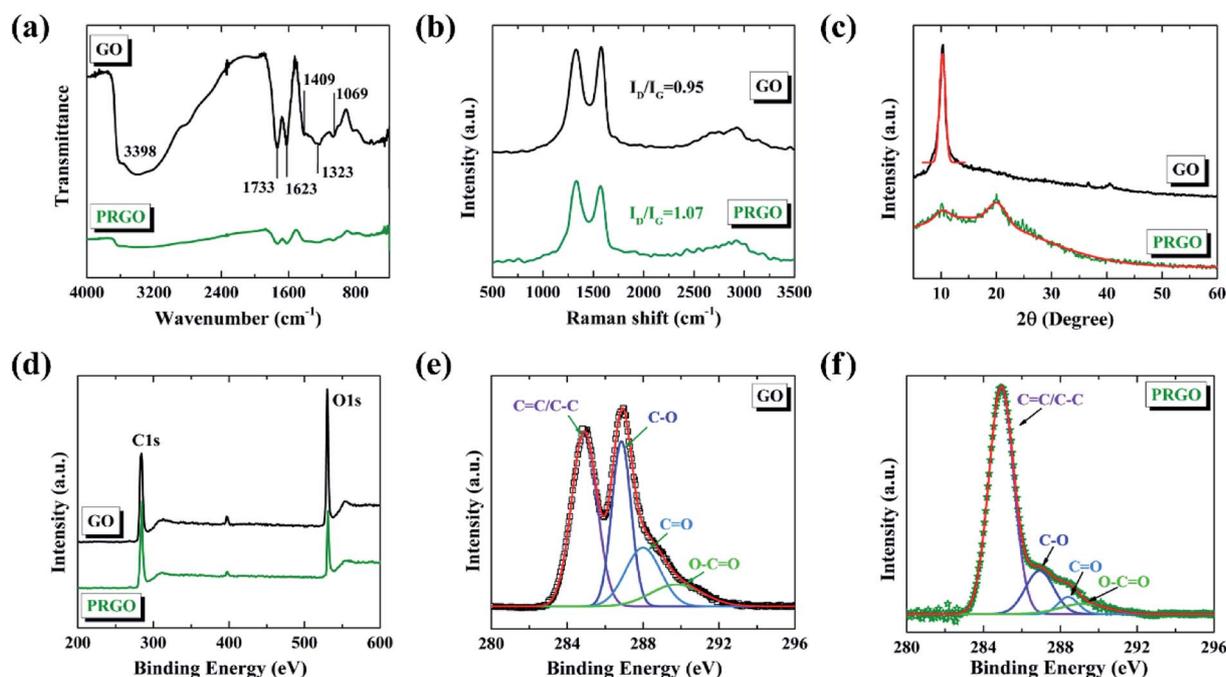

Fig. 1 Chemical characterizations of GO and PRGO. FTIR spectra (a), Raman spectra (b), and XRD patterns (c) of GO and PRGO with irradiation duration of 72 hours. (d) XPS survey spectra and (e and f) curve fits of C1s spectra of GO and PRGO with irradiation duration of 72 h.

I_D/I_G ratio from 0.95 for GO to 1.07 for PRGO indicates the decreased sizes but the increased numbers of sp^2 frameworks.[40] The XRD patterns of GO and PRGO are shown in Fig. 1c. GO exhibits a sharp peak at 10.24°, corresponding to an interlayer separation of 0.863 nm. For PRGO, this peak almost disappears whereas a broad and weak peak at 20.20° becomes prominent. The new peak corresponds to an interlayer spacing of 0.439 nm. The significant reduction of the interlayer spacing further indicates the removal of oxygen-containing functional groups.[41]

Here, we also used XPS to qualify the degree of photoreduction. The C/O ratio can be determined from the atomic percentage by the survey XPS spectra,[42] as shown in Fig. 1d. The C/O ratio of GO before and after solar light irradiation increases from 2.47 to 6.79, further revealing the removal of oxygen-containing functional groups from GO. Fig. 1e and f present the C1s deconvolution spectra of GO and PRGO, respectively. Both spectra can be curve-fitted into four peaks. The binding energies of the fitted peaks are about 284.9, 286.9, 288.4, and 289.4 eV, corresponding to C=C/C–C, C–O (hydroxyl and epoxy), C=O (carbonyl), and O=C–O (carboxyl) species.[43] Compared with GO, the oxygen-bound C components in PRGO, especially the peak of C–O, are decreased sharply in intensity. This further confirms that most of the oxygen functional groups have been removed by solar light irradiation.

The surface morphologies of GO before and after solar light irradiation were characterized by AFM, SEM, and TEM, as shown in Fig. 2. It can be seen that GO nano-sheets are exfoliated into monolayers with lateral size in the region of 2–4 μm and height of ~1.5 nm (Fig. 2a), coinciding with previous works.[37,44] After solar light irradiation, the lateral size of nano-sheets slightly decreased. As shown in Fig. 2b, the height of

PRGO was decreased to ~1.0 nm, indicating the effective removal of functional groups on the basal plane of GO. Fig. 2c–f present the SEM and TEM images of GO and PRGO. GO presents a single- or a few-layer microstructure with wrinkles on the surface, which may be due to large amounts of functional groups.[45,46] These groups expand the interlayer distance of graphite and result in the wrinkle phenomenon, in accordance with the XRD results. However, PRGO presents a different morphology as fluffy and transparent layers with rich wrinkles and fluctuation.[45] The fluctuation may be essential to sustain the thermodynamics stability of two-dimensional natural crystal structure of graphene sheets. These disordered reduced graphene sheets could connect as a three-dimensional porous network, which will improve the adsorption of contaminants. This hypothesis can be proven by the measurement of surface areas using the BET technique (Fig. S4†), where the surface area of PRGO (62.8 m^2 g^{-1}) is higher than that of GO (20.2 m^2 g^{-1}). Furthermore, energy dispersive X-ray spectroscopy (EDS) was also performed to analyze the chemical components of GO and PRGO, as shown in Fig. S5.† From the analysis, we can find that the main elements on the prepared samples are C and O. The significant decrease of O element further reveals the removal of oxygen functional groups. Note that the atomic percentage of C/O ratio increasing from 1.58 to 5.16 agrees reasonably well with the analysis from the survey XPS spectra.

3.2 Adsorption kinetics and isotherms in single-component system

3.2.1 Adsorption kinetics. To elucidate the mechanisms of contaminant binding processes as well as to understand the rate-controlling step, the adsorption kinetics was firstly
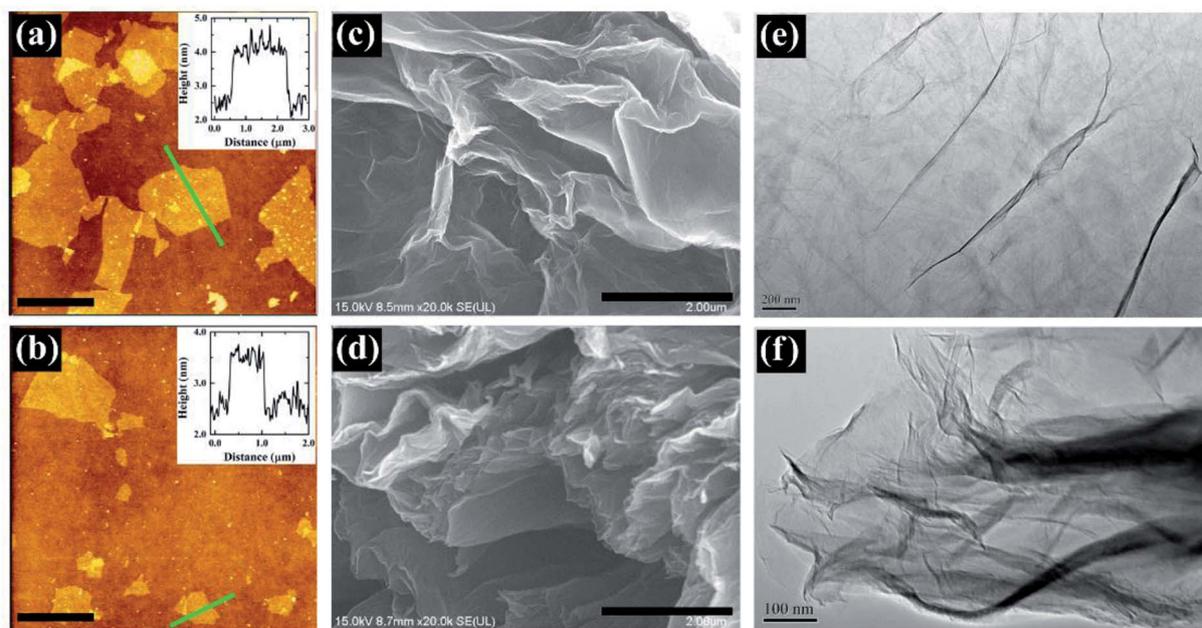

Fig. 2 (a and b) AFM, (c and d) SEM, and (e and f) TEM images of GO and PRGO flakes. (a, c and e) Results for the original GO. (b, d and f) Results for PRGO after irradiation with solar light for 72 hours. The insets shown in (a) and (b) are the height profiles of the selected lines. Scale bar: 2 μm for (a–d).

investigated by measuring the time-dependent adsorption behaviors, as shown in Fig. 3. The adsorption of OII on PRGO is rapidly increased in the first 5 min and almost reaches equilibrium in less than half an hour. However, the adsorption on GO is relatively slow and reaches equilibrium at about 2 hours, as shown in Fig. 3a. On the other hand, the adsorption rates of MB and Pb^{2+} are both faster than that of OII, for which the adsorption equilibrium is reached in the first 30 min for all GO and PRGO materials. To get an insight into the adsorption processes and to determine the kinetic parameters, the experimental data are fitted by the pseudo-second-order model.

The pseudo-second-order model is generally used to depict the chemisorption process with a rate-limiting step,[47] which can be represented as the equation:

$$\frac{t}{q_t} = \frac{t}{q_e} + \frac{1}{k_2 q_e^2} \tag{2}$$

where q_e is the adsorption capacity at equilibrium and q_t is the amount of contaminant adsorbed at time t. The k_2 parameter in $g\,(mg\,min)^{-1}$ denotes the rate constant of the pseudo-second-order kinetic model. Specifically, V_0 represents the adsorption rate at initial time,[48] where

$$V_0 = k_2 q_e^2 \tag{3}$$

The results are presented in Table 1. The linear correlation coefficients (R^2) for these adsorption conditions are between 0.991 and 0.999, indicating that the experimental data are in good agreement with the pseudo-second-order model. The adsorption rates of GO and PRGO for MB and Pb^{2+} are significantly higher than those for OII. Furthermore, with increasing reduction degree, the adsorption rate of MB is slightly decreased and that of OII is clearly increased, while the adsorption rate of Pb^{2+} shows negligible change.

3.2.2 Adsorption isotherms. The adsorption capacities of the ionic dyes and Pb^{2+} onto GO and PRGO were then determined by adsorption isotherm studies. Here, the adsorption capacities and the equilibrium concentrations were obtained after shaking the mixture of contaminants and absorbents for 24 hours at room temperature (25 °C). As shown in Fig. 4b and c, the adsorption capacities of MB and Pb^{2+} onto GO and PRGO

Table 1 Parameters of the pseudo-second-order kinetic model for the adsorption of OII, MB, and Pb^{2+} on GO and PRGO

		GO	PRGO-1	PRGO-2	PRGO-3
OII	q_e (mg g^{-1})	4.87	15.0	21.9	31.9
	k_2 (g (mg min)$^{-1}$)	0.05	0.29	0.35	0.40
	V_0 (mg (g min)$^{-1}$)	0.24	4.3	7.8	12.9
	R^2	0.998	0.999	0.999	0.999
MB	q_e (mg g^{-1})	149	148	148	149
	k_2 (g (mg min)$^{-1}$)	6.9	3.6	4.7	3.3
	V_0 (mg (g min)$^{-1}$)	1024	537	847	505
	R^2	0.991	0.994	0.996	0.993
Pb^{2+}	q_e (mg g^{-1})	290	296	293	294
	k_2 (g (mg min)$^{-1}$)	4.9	4.5	3.9	4.1
	V_0 (mg (g min)$^{-1}$)	1425	1446	1161	1198
	R^2	0.995	0.993	0.997	0.992

varying as the equilibrium concentrations show similar behaviors, indicating that their maximum adsorption capacities are comparable. However, for OII, not only are the adsorption capacities distinct from GO to PRGO, but also the adsorption behaviors are quite different from those for MB and Pb^{2+}. To determine the maximum adsorption capacity under each condition, the Langmuir model is used to analyze the experimental data. The Langmuir model involves a monolayer adsorption process on a uniform surface with no interaction among the adsorbed molecules (dyes).[47] It can be expressed as follows:

$$\frac{C_e}{q_e} = \frac{C_e}{q_{max}} + \frac{1}{q_{max}}\frac{1}{K_L} \tag{4}$$

where C_e is the adsorption equilibrium concentration (mg L^{-1}), q_e is the corresponding adsorption amount at this dye concentration (mg g^{-1}), q_{max} is the maximum adsorption capacity in mg g^{-1}, corresponding to complete monolayer coverage, and K_L is the Langmuir constant in L mg^{-1}, related to the affinity of the binding sites and energy of adsorption. The calculated results are shown in Table 2. The linear correlation coefficients (R^2) for these adsorption conditions are between 0.965 and 0.997, indicating that the experimental data are in good agreement with the Langmuir model. From Table 2, we
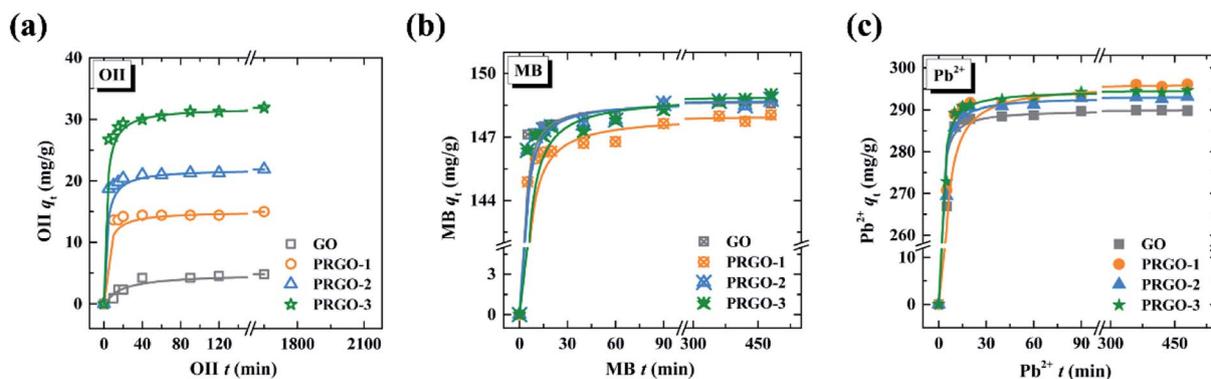

Fig. 3 Adsorption kinetics of GO and PRGO-1, -2, and -3 for (a) OII, (b) MB, and (c) Pb^{2+}. The solid lines are the pseudo-second-order model simulations.
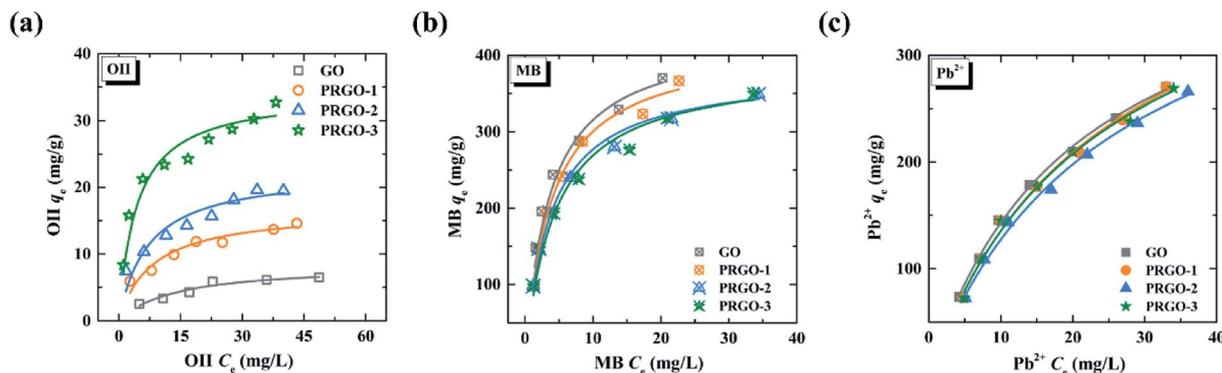
Fig. 4 Adsorption isotherms of GO and PRGO-1, -2, and -3 for (a) OII, (b) MB, and (c) Pb^{2+}. The solid lines are the Langmuir model simulations.

Table 2 Parameters of the Langmuir isotherm for the adsorption of OII, MB, and Pb^{2+} on GO and PRGO

		GO	PRGO-1	PRGO-2	PRGO-3
OII	q_{max} (mg g^{-1})	8.4	16.8	22.6	32.5
	K_L (L mg^{-1})	7.5×10^{-2}	1.1×10^{-1}	1.3×10^{-1}	2.1×10^{-1}
	R^2	0.971	0.975	0.965	0.982
MB	q_{max} (mg g^{-1})	429	415	380	386
	K_L (L mg^{-1})	0.28	0.26	0.27	0.23
	R^2	0.988	0.993	0.997	0.993
Pb^{2+}	q_{max} (mg g^{-1})	431	459	444	446
	K_L (L mg^{-1})	0.5×10^{-1}	4.2×10^{-1}	4.0×10^{-1}	4.3×10^{-1}
	R^2	0.995	0.980	0.985	0.979

can see that the adsorption capacity of OII on GO is only 8.4 mg g^{-1}. With increasing reduction degree (increasing of irradiation duration), the adsorption capacity of OII is gradually increased. Note that the adsorption capacity of PRGO-3 is 32.5 mg g^{-1}, which is almost 4-fold larger than that of GO. In contrast, the adsorption capacity of MB on PRGO is slightly lower than that on GO. While the effect of the reduction of GO on the adsorption of Pb^{2+} can be ignored. The mechanism behind these phenomena will be discussed in the following. One thing that should be mentioned is that the adsorption isotherms of OII, MB and Pb^{2+} on GO and PRGO can also be well analyzed by Freundlich and Temkin models,[49,50] as presented in Fig. S6, Tables S1 and S2.† The results further reveal that the adsorption of these three contaminants on GO and PRGO are favorable Langmuir adsorption processes and exothermic in nature.

3.3 Co-adsorption investigations of OII-MB binary system

Co-adsorption investigations of the OII-MB binary system have been classified into two categories: the adsorption isotherm of MB in the presence of OII, and the adsorption isotherm of OII in the presence of MB. These two categories are designated in the forms of MB/OII and OII/MB for short, as discussed in Section 2.4.2.

3.3.1 Co-adsorption isotherms in MB/OII system. The adsorption capacities of MB as a function of OII concentration are presented in Fig. 5a. The initial concentration of MB was fixed at 200 mg L^{-1}, while that of OII was changed from 0 to

300 mg L^{-1}. It can be seen that with increasing OII concentration, the adsorption capacities of MB on GO and PRGO are mildly increased, with the maximum capacity at an OII concentration of $\sim$133 mg L^{-1}, and then slightly decreased. However, comparing with the absolute adsorption capacities, the variations are small. Dividing the variations by the adsorption capacity of MB on GO in the absence of OII, the variations are in the region of 2.1% and -3.4%, as shown at the bottom of Fig. 5a. Furthermore, although the adsorption capacities of MB on PRGO are slightly smaller than that on GO in the absence of OII, as presented in Table 2, GO and PRGO give almost the same adsorption capacities when the concentrations of OII are larger than 133 mg L^{-1}.

On the other hand, to compare the maximum adsorption capacities of MB in the absence/presence of OII, we also obtained the adsorption isotherms of MB under different OII concentrations, as shown in Fig. 5b. Note that the adsorption isotherms of MB in the presence of OII (100, 200, and 300 mg L^{-1}) are similar to that in the absence of OII (0 mg L^{-1}); thus they are also analyzed by the Langmuir model. The maximum adsorption capacities are shown in Fig. 5c (the corresponding fitted results can be found in Fig. S7 and Table S3†). At a glance, the maximum adsorption capacities of MB on GO and PRGO in the absence and presence of OII have no significant difference, and they are all around 400 mg g^{-1}.

To gain an insight into the co-adsorption behaviors, the ratio of adsorption capacity R_q is often used:[29,36]

$$R_q = \frac{Q_{b,i}}{Q_{m,i}} \tag{5}$$

where $Q_{b,i}$ is the adsorbed amount of the i-th adsorbate from the binary solution, and $Q_{m,i}$ is that from the single-component solution at an identical condition. R_q represents the co-adsorption as being either synergism ($R_q > 1$), indifference ($R_q = 1$), or antagonism ($R_q < 1$).[29] That is, for $R_q > 1$, the presence of co-adsorbate will improve the adsorption capacity for the target adsorbate; while for $R_q < 1$, the co-adsorbate will compete with the target adsorbate, resulting in a decrease of the adsorption capacity for the target adsorbate. In this section, MB is the target adsorbate, while OII is the co-adsorbate. To investigate the co-adsorption as well as the influence of the reduction
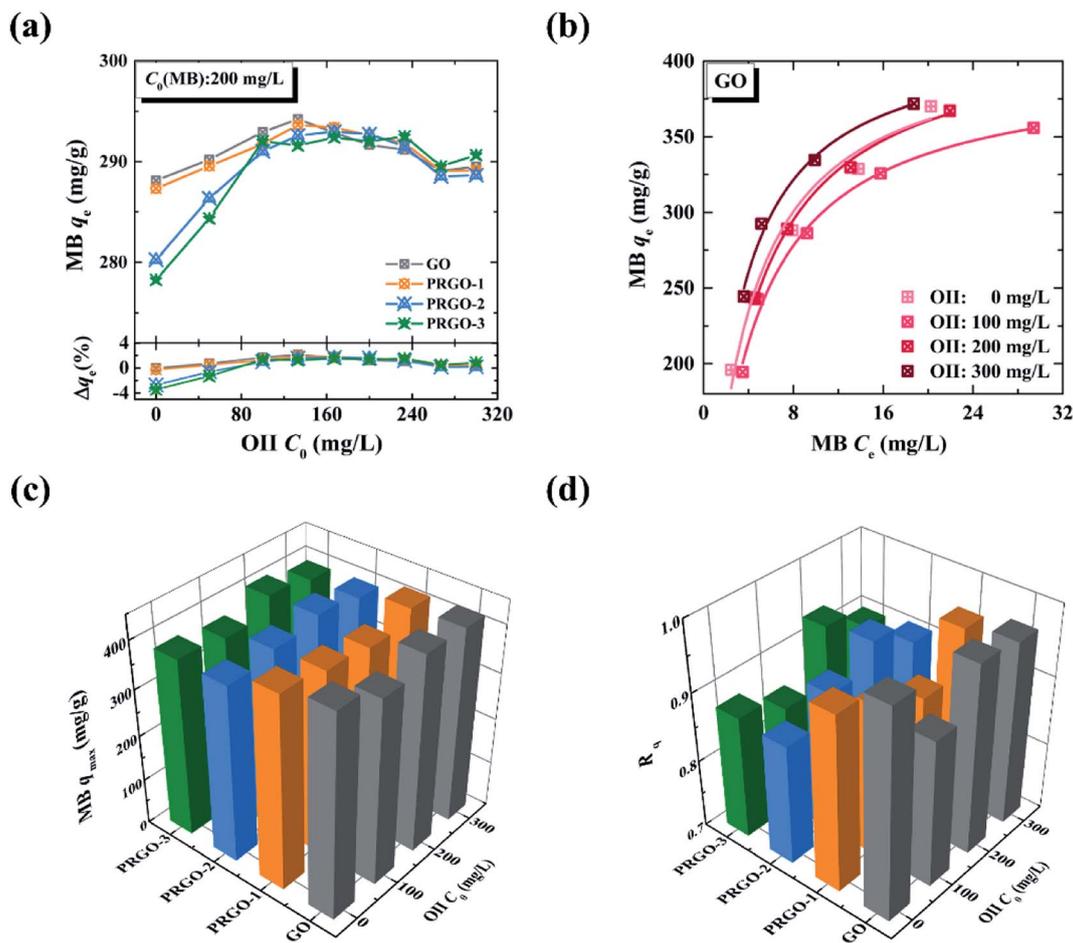
Fig. 5 Co-adsorption of MB in the presence of OII. (a) The equilibrium adsorption capacities of MB on GO and PRGO as a function of OII concentration. (b) The adsorption isotherms of MB on GO under different OII concentrations. The solid lines are the Langmuir model simulations. (c) The maximum adsorption capacities of MB on GO and PRGO in the presence of OII. (d) The corresponding R_q of MB on GO and PRGO in the presence of OII.

process, here $Q_{m,i}$ is set as the adsorption capacity of MB on GO in the absence of OII. The corresponding results are presented in Fig. 5d (all the values of R_q are presented in Table S4†). It can be determined that the R_q values of GO in the presence of OII are in the region of 0.913 to 0.975, indicating that the existence of OII can slightly inhibit the adsorption of MB on GO. On the other hand, the R_q values of PRGO in the absence of OII are in the region of 0.875 to 0.954, indicating that the reduction process will suppress the adsorption of MB as well, consistent with the results presented in Table 2. Furthermore, the R_q values of PRGO in the presence of OII are in the region of 0.852 to 0.943, in accordance with the results discussed above.

3.3.2 Co-adsorption isotherms in OII/MB system. The adsorption behaviors of OII varying as a function of MB concentration are presented in Fig. 6. In contrast with MB, the adsorption capacities of OII are significantly enhanced in the presence of MB, as shown in Fig. 6a. In the absence of MB, the adsorption of OII by PRGO is higher than that by GO, as we discussed for the single-component experiment. However, as the concentration of MB increases from 0 mg L^{-1} to 167 mg L^{-1}, the adsorption capacity of OII on GO increases from 8.4 mg g^{-1}

to 126.6 mg g^{-1}, an enhancement of 15-fold. The enhanced adsorption capacity will remain at this value when the concentration of MB is further increased. On the other hand, the difference between GO and PRGO gradually disappears. Fig. 6b presents the adsorption isotherms of OII on PRGO-1 in the presence of MB (the adsorption isotherms of other materials can be found in Fig. S8†). Note that the adsorption isotherms of OII are different between the absence (0 mg L^{-1}) and presence of MB. Nevertheless, when the concentrations of MB are 200 mg L^{-1} and 300 mg L^{-1}, the adsorption behaviors are similar, indicating that the adsorption capacity of OII cannot be further enhanced by continuing to increase the concentration of MB.

The maximum adsorption capacities of OII on GO and PRGO in the presence of MB, and the corresponding ratios R_q are shown in Fig. 6c and d, respectively (the maximum adsorption capacities were determined by the Langmuir model, and the detailed fitted results can be found in Tables S5 and S6†). For GO, R_q is 34.3 when the MB concentration is 300 mg L^{-1}, indicating that a remarkable synergistic effect is observed for the removal of OII by GO in the presence of MB. This yields an
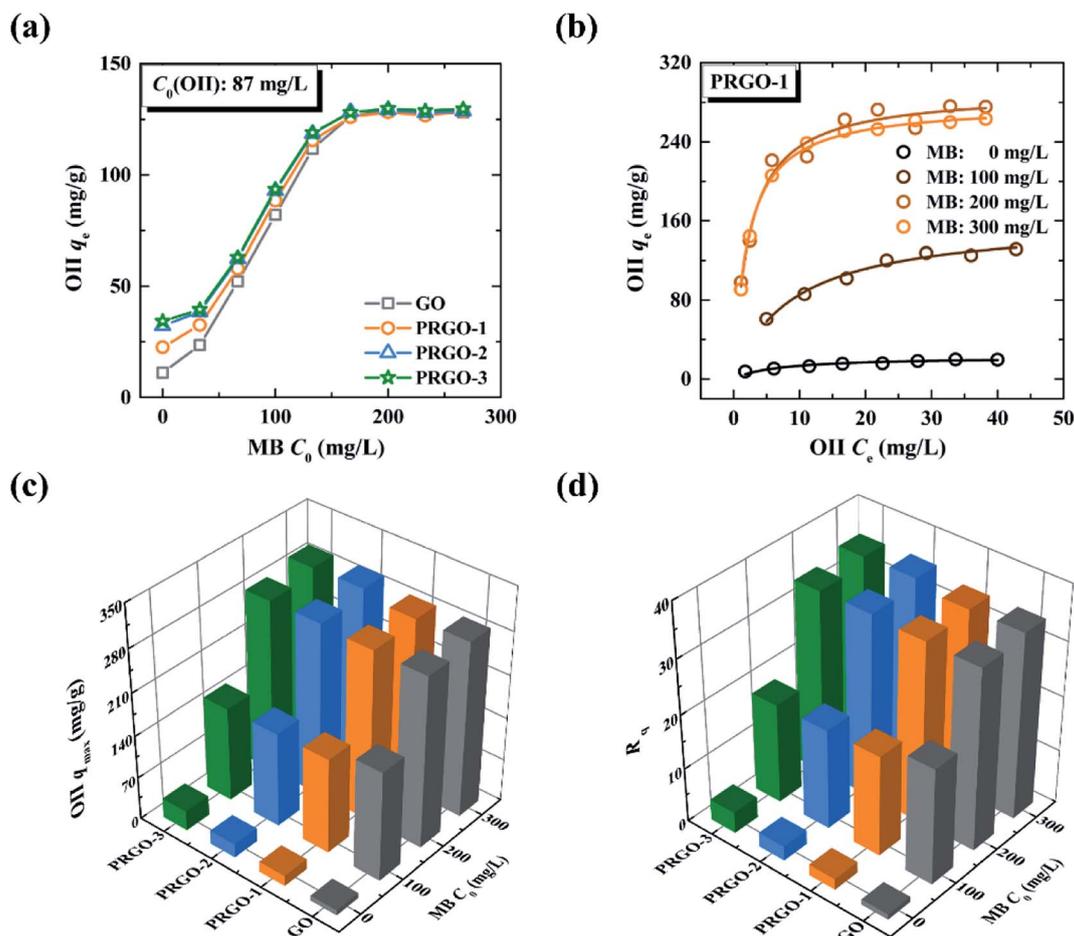
Fig. 6 Co-adsorption of OII in the presence of MB. (a) The equilibrium adsorption capacities of OII on GO and PRGO as a function of MB concentration. (b) The adsorption isotherms of OII on PRGO-1 under different MB concentrations. The solid lines are the Langmuir model simulations. (c) The maximum adsorption capacities of OII on GO and PRGO in the presence of MB. (d) The corresponding ratios R_q of OII on GO and PRGO in the presence of MB.

exceptionally high adsorption capacity of OII. On the other hand, in the presence of MB, R_q of PRGO is almost the same as that of GO. This result hints that the promoting effect for OII by the reduction process can be ignored, comparing with the synergistic effect from simultaneous adsorption of MB.

3.4 Co-adsorption investigations of OII-Pb^{2+} binary system

3.4.1 Co-adsorption isotherms in OII/Pb^{2+} system. Here the anionic dye OII and Pb^{2+} were used as model adsorbates to investigate the co-adsorption in dye-metal ion binary system. Firstly, the adsorption capacities of OII on GO and PRGO in the presence of Pb^{2+} were investigated. As shown in Fig. 7a, when the initial concentration of OII was fixed at 100 mg L^{-1}, the adsorption capacities of GO and PRGO all increase with increasing Pb^{2+} concentration. This phenomenon is analogous to the adsorption of OII in the presence of MB, as shown in Fig. 6a. In addition, the adsorption isotherms of OII on PRGO-2 shown in Fig. 7b are similar to those on PRGO-1 shown in Fig. 6b. However, in contrast with the presence of MB, the deeper the reduction of GO, the higher the adsorption capacity of OII. This conclusion can be further explored by the maximum

adsorption capacities of OII on GO and PRGO and the corresponding ratios in the presence of Pb^{2+}, as shown in Fig. 7c and d, respectively (the detailed fitted results can be found in Tables S7 and S8†). For GO, the adsorption capacity of OII is improved from 8.4 mg g^{-1} to 85.3 mg g^{-1}, with the concentration of Pb^{2+} increasing from 0 to 300 mg L^{-1}. On the other hand, with the concentration of Pb^{2+} fixed, the adsorption capacity of GO to PRGO-3 is gradually improved. Taking Pb^{2+} at 100 mg L^{-1} as an example, the adsorption capacities of GO and PRGO-1, -2, and -3 are 61.1, 68.0, 73.3, and 86.2 mg g^{-1}, respectively. The corresponding R_q are 7.3, 8.1, 8.7, and 10.3, respectively. These results indicate that the superior adsorption capacity of OII on PRGO results from the synergistic effect of the reduction process and the presence of Pb^{2+}. Consequently, in this work, the maximum R_q has reached 12.5 for PRGO with a Pb^{2+} concentration of 300 mg L^{-1}. It is noteworthy that the linear correlation coefficients (R^2) of PRGO are better than those of GO (see Table S7† for detailed parameters), hinting that the Langmuir model is more appropriate for PRGO than for GO.

3.4.2 Co-adsorption isotherms in Pb^{2+}/OII system. In contrast to the dramatic synergistic effect for OII in the presence
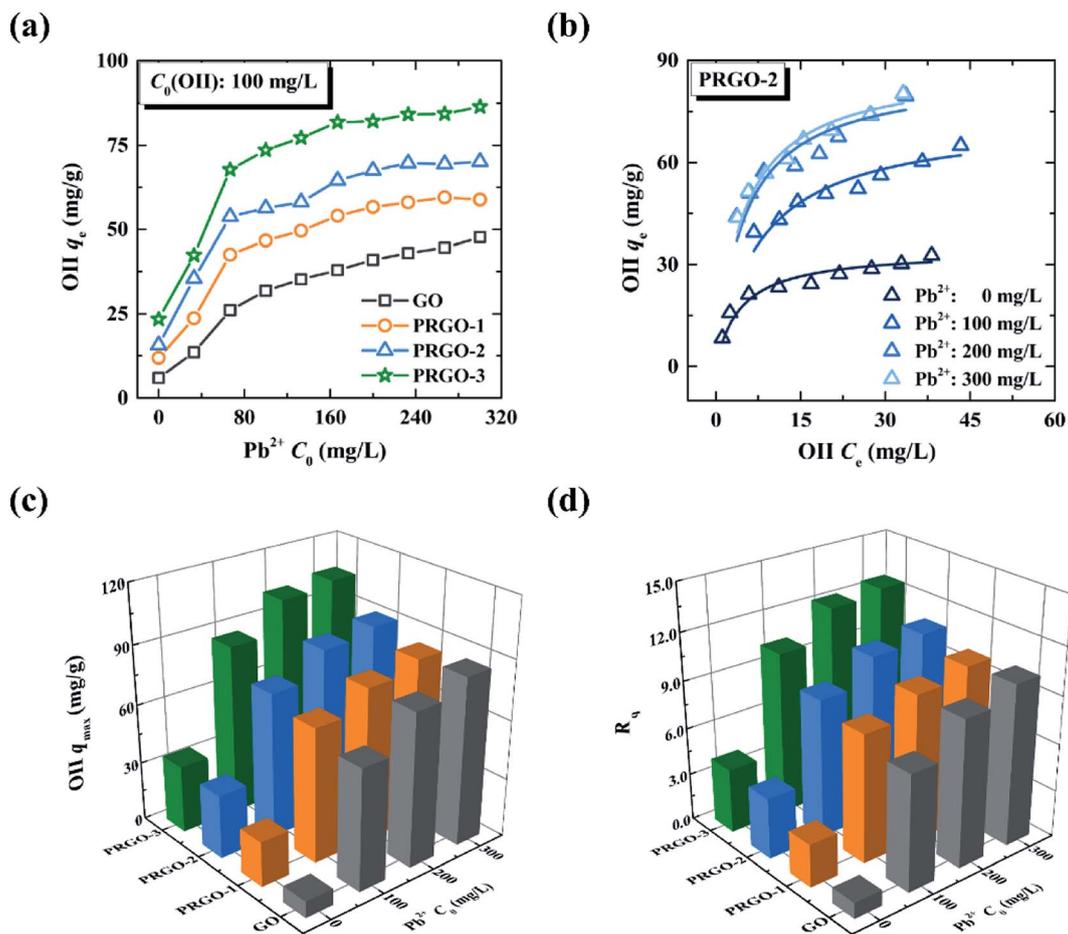
Fig. 7 Co-adsorption of OII in the presence of Pb^{2+}. (a) The equilibrium adsorption capacities of OII on GO and PRGO as a function of Pb^{2+} concentration. (b) The adsorption isotherms of OII on PRGO-2 under different Pb^{2+} concentrations. The solid lines are the Langmuir model simulations. (c) The maximum adsorption capacities of OII on GO and PRGO in the presence of Pb^{2+}. (d) The corresponding ratios R_q of OII on GO and PRGO in the presence of Pb^{2+}.

of Pb^{2+}, the adsorption of Pb^{2+} is suppressed in the presence of OII dye. As shown in Fig. 8a, the adsorption capacity of Pb^{2+} is decreased from ~ 350 mg g^{-1} to ~ 220 mg g^{-1}, neither GO nor PRGO making much difference. Note that the adsorption capacity almost remains at the same value when further increasing the OII concentration. Also noteworthy is that the adsorption isotherms of Pb^{2+} on GO in the presence of OII can be analyzed by Langmuir and Freundlich models (as shown in Fig. S10†), while those on PRGO can only be fitted by the Freundlich model (see Table S9† for detailed parameters). Thus the maximum adsorption capacities are replaced by the equilibrium adsorption capacities, as shown in Fig. 8c (see Table S10† for detailed parameters). In this case, the adsorption capacities of PRGO are still larger than those of GO. Consequently, R_q are in the range 0.696 to 0.766 for GO, and 0.724 to 0.874 for PRGO, indicating the existence of a competitive effect for Pb^{2+} in the presence of OII.

3.5 Adsorption mechanisms

Based on the adsorption investigations of ionic dyes and heavy metal ion onto GO and PRGO in single-component and binary systems, we can find that the reduction of GO can improve the adsorption capacity of anionic OII dye, while it has a negligible effect for both cationic MB and positively charged Pb^{2+}. More importantly, the presence of both MB and Pb^{2+} can strongly enhance the adsorption of OII (synergistic effect), while the presence of OII inhibits the adsorption of MB and Pb^{2+} (antagonistic effect). According to previous work,[35] MB mildly enhanced the adsorption of Pb^{2+}, while the presence of Pb^{2+} will suppress the adsorption of MB. These phenomena can be understood from two aspects: the effect of the reduction process and the presence of co-adsorbent.

Generally, the adsorption mechanisms of contaminants on graphene-based materials can be considered from two aspects: the electrostatic interaction between the contaminants and the oxygen-containing functional groups of graphene-based materials, as well as the π–π interaction between the aromatic structure of the dyes and the π-conjugation frameworks of graphene sheets.[32,51,52] Meanwhile, original GO is highly negatively charged, resulting from the abundant oxygen-containing functional groups on its basal plane. While the negative
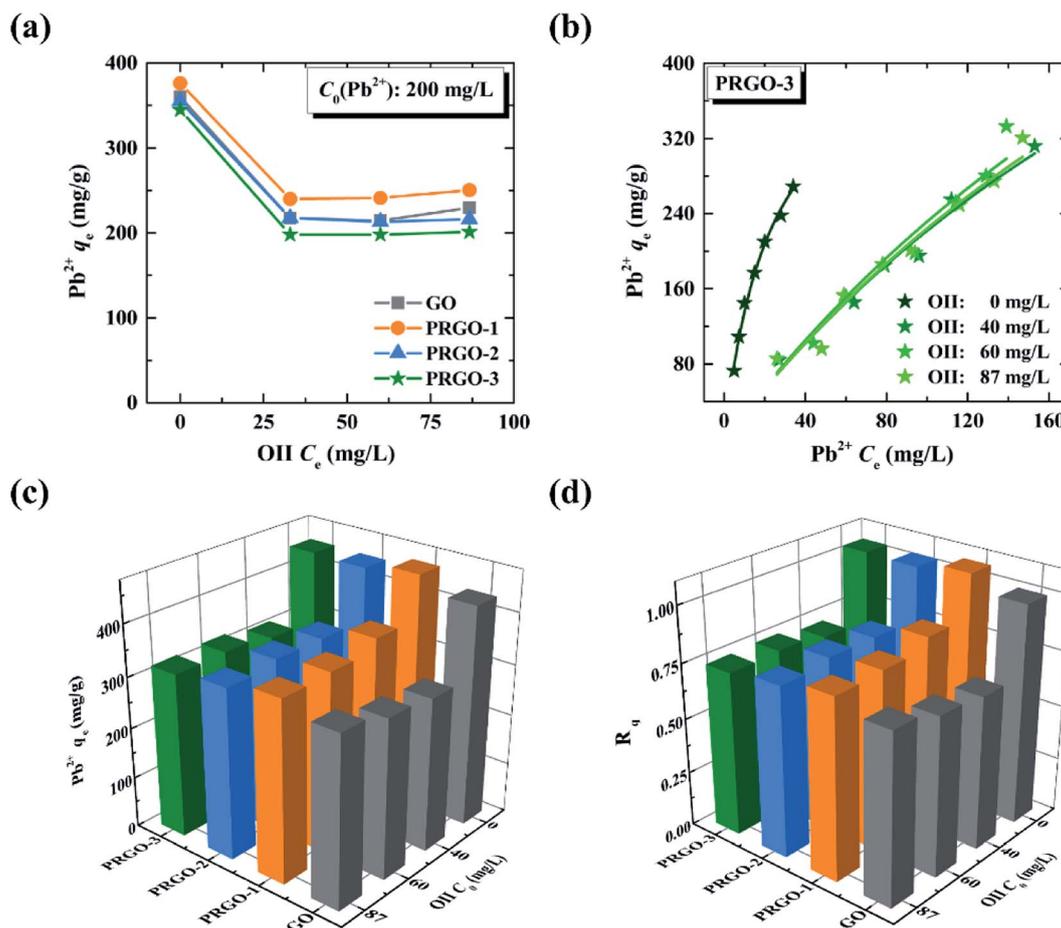
Fig. 8 Co-adsorption of Pb^{2+} in the presence of OII. (a) The equilibrium adsorption capacities of Pb^{2+} on GO and PRGO as a function of OII concentration. (b) The adsorption isotherms of Pb^{2+} on PRGO-3 under different OII concentration. The solid lines are the Langmuir model simulations. (c) The maximum adsorption capacities of Pb^{2+} on GO and PRGO in the presence of OII. (d) The corresponding ratios R_q of Pb^{2+} on GO and PRGO in the presence of OII.

charge of PRGO will be less, due to the removal of functional groups by photoreduction.[53,54] Therefore, GO has extremely low adsorption capacity for anionic OII dye, due to the strong electrostatic repulsion interaction between negative GO and anionic OII. This repulsion will become weak after photoreduction. Thus, the adsorption capacity of anionic OII gradually enhances, during GO conversion into PRGO by photoreduction. For MB, both π–π interaction and electrostatic interaction will contribute to its adsorption capacity. For GO, the electrostatic interaction may dominate the adsorption process, due to the highly negatively charged GO and positively charged MB. For PRGO, the π–π interaction may be predominant, due to the restoration of π-conjugation frameworks during photoreduction.[37] Consequently, a competition between these two interactions occurs, resulting in a negligible effect of the reduction process. This interpretation is appropriate for the adsorption of Pb^{2+} as well, where the main adsorption mechanisms between Pb^{2+} and graphene-based materials are electrostatic interaction and cation–π interaction.[55,56] Thus, the adsorption capacities for both MB and Pb^{2+} present no obvious change from GO to PRGO.

In the MB/OII binary system, OII will occupy some adsorption sites through π–π interaction, which will inhibit the adsorption of MB. However, comparing with the adsorption capacity of MB on GO of 429 mg g^{-1}, that of OII is only 8.4 mg g^{-1}. Thus the presence of OII leads to a mildly antagonistic effect on the adsorption of MB. In contrast, in the OII/MB binary system, the presence of MB remarkably enhances the adsorption of OII, because the electronegativity of GO after adsorption of MB is significantly decreased. The decrease of the repulsion interaction between OII and GO will remarkably enhance the adsorption of OII. It can also explain the synergistic effect of OII in the presence of Pb^{2+}. On the other hand, the π–π interaction between OII and GO will suppress the cation–π interaction between Pb^{2+} and π-conjugation frameworks of graphene-based materials, and thus the presence of OII shows an antagonistic effect on Pb^{2+}.

4. Conclusion

In order to simultaneously remove anionic and cationic dyes as well as heavy metal ions from wastewater, GO and its reduced

counterpart PRGO were prepared, where PRGO was synthesized by a green and cost-free method based on the solar light irradiation of GO suspensions. FTIR, Raman, XRD, XPS, AFM, SEM, and TEM studies show that the oxygen-containing functional groups had been successfully removed from PRGO. Compared with the original GO, the adsorption capacity of OII on PRGO is improved by 4 times in a single-component system, while that of MB and Pb^{2+} show negligible change. In a binary system, a remarkable synergistic effect has been determined for the adsorption of anionic OII dye, in the presence of either cationic MB or positively charged Pb^{2+}. The enhancement reached 34.3- and 12.5-fold, respectively. This synergistic effect may result from the decrease of the electronegativity of GO. On the other hand, in the presence of OII, the adsorption capacity of neither MB nor Pb^{2+} is suppressed. The antagonistic effect originates from the occupation of adsorption sites by OII through π–π interaction, where MB will adsorb on GO or PRGO by π–π interaction, and Pb^{2+} will adsorb through cation–π interaction. Consequently, the maximum adsorption capacity of OII by PRGO has reached 296 mg g^{-1} in this work, which is comparable to the adsorption by activated carbon previously reported.[57,58] Hence, we provide a new insight for the treatment of anionic dyes and the removal of coexisting contaminants in polluted wastewater by GO and PRGO, which can be considered as alternative adsorbents to conventional carbon-based adsorbents for removing contaminants from wastewater.

Conflicts of interest

The authors declare no competing financial interest.

Acknowledgements

References

1 I. Ali, Chem. Rev., 2012, 112, 5073–5091.
2 J. Eliasson, Nature, 2015, 517, 6.
3 M. Yusuf, F. M. Elfghi, S. A. Zaidi, E. C. Abdullah and M. A. Khan, RSC Adv., 2015, 5, 50392–50420.
4 M. R. S. Kebria, M. Jahanshahi and A. Rahimpour, Desalination, 2015, 367, 255–264.
5 J. Labanda, J. Sabaté and J. Llorens, J. Membr. Sci., 2009, 340, 234–240.
6 G. C. Silva, V. S. T. Ciminelli, A. M. Ferreira, N. C. Pissolati, P. R. P. Paiva and J. L. López, Mater. Res. Bull., 2014, 49, 544–551.
7 İ. Duru, D. Ege and A. R. Kamali, J. Mater. Sci., 2016, 51, 6097–6116.
8 M. Jafari, M. R. Rahimi, M. Ghaedi and K. Dashtian, Chem. Eng. Res. Des., 2017, 125, 408–421.
9 A. A. Oladipo and M. Gazi, J. Taiwan Inst. Chem. Eng., 2015, 47, 125–136.
10 B. Qiu, H. Gu, X. Yan, J. Guo, Y. Wang, D. Sun, Q. Wang, M. Khan, X. Zhang, B. L. Weeks, D. P. Young, Z. Guo and S. Wei, J. Mater. Chem. A, 2014, 2, 17454–17462.
11 B. Qiu, Y. Wang, D. Sun, Q. Wang, X. Zhang, B. L. Weeks, R. O'Connor, X. Huang, S. Wei and Z. Guo, J. Mater. Chem. A, 2015, 3, 9817–9825.
12 G. Z. Kyzas, P. I. Siafaka, E. G. Pavlidou, K. J. Chrissafis and D. N. Bikiaris, Chem. Eng. J., 2015, 259, 438–448.
13 H. C. Yang, J. L. Gong, G. M. Zeng, P. Zhang, J. Zhang, H. Y. Liu and S. Y. Huan, J. Colloid Interface Sci., 2017, 505, 67–78.
14 V. Vimonses, S. Lei, B. Jin, C. W. K. Chow and C. Saint, Chem. Eng. J., 2009, 148, 354–364.
15 K. Liu, L. Zhang, T. Cao, C. Jin, D. Qiu, Q. Zhou, A. Zettl, P. Yang, S. G. Louie and F. Wang, Nat. Commun., 2014, 5, 4966.
16 G. Ersan, O. G. Apul, F. Perreault and T. Karanfil, Water Res., 2017, 126, 385–398.
17 W. Peng, H. Li, Y. Liu and S. Song, J. Mol. Liq., 2017, 230, 496–504.
18 I. Khurana, A. Saxena, Bharti, J. M. Khurana and P. K. Rai, Water, Air, Soil Pollut., 2017, 228, 180.
19 V. Chandra and K. S. Kim, Chem. Commun., 2011, 47, 3942–3944.
20 L. Sun, H. Yu and B. Fugetsu, J. Hazard. Mater., 2012, 203–204, 101–110.
21 Y. Zhu, H. Ji, H.-M. Cheng and R. S. Ruoff, Natl. Sci. Rev., 2018, 5, 90–101.
22 W. Ren and H. M. Cheng, Nat. Nanotechnol., 2014, 9, 726–730.
23 O. G. Apul, Q. Wang, Y. Zhou and T. Karanfil, Water Res., 2013, 47, 1648–1654.
24 N. Cai and P. Larese-Casanova, J. Colloid Interface Sci., 2014, 426, 152–161.
25 S. Chang, C. Lu and K.-Y. A. Lin, Appl. Surf. Sci., 2015, 326, 187–194.
26 F. Wang, X. Lu, W. Peng, Y. Deng, T. Zhang, Y. Hu and X.-y. Li, ACS Omega, 2017, 2, 5378–5384.
27 L. Chen, Y. Li, Q. Du, Z. Wang, Y. Xia, E. Yedinak, J. Lou and L. Ci, Carbohydr. Polym., 2017, 155, 345–353.
28 Z. Y. Sui, Y. Cui, J. H. Zhu and B. H. Han, ACS Appl. Mater. Interfaces, 2013, 5, 9172–9179.
29 Q. Kong, C. Wei, S. Preis, Y. Hu and F. Wang, Environ. Sci. Pollut. Res. Int., 2018, 25, 21164–21175.
30 M. Lv, L. Yan, C. Liu, C. Su, Q. Zhou, X. Zhang, Y. Lan, Y. Zheng, L. Lai, X. Liu and Z. Ye, Chem. Eng. J., 2018, 349, 791–799.
31 J. Xiao, J. Zhang, W. Lv, Y. Song and Q. Zheng, Carbon, 2017, 123, 354–363.
32 J. Xiao, W. Lv, Z. Xie, Y. Tan, Y. Song and Q. Zheng, J. Mater. Chem. A, 2016, 4, 12126–12135.
33 J. Xiao, W. Lv, Z. Xie, Y. Song and Q. Zheng, J. Mater. Sci., 2017, 52, 5807–5821.

34 J.-H. Deng, X.-R. Zhang, G.-M. Zeng, J.-L. Gong, Q.-Y. Niu and J. Liang, *Chem. Eng. J.*, 2013, **226**, 189–200.

35 L. Liu, Y. Zhang, Y. He, Y. Xie, L. Huang, S. Tan and X. Cai, *RSC Adv.*, 2015, **5**, 3965–3973.

36 M. Zheng, Y. Ahn, Y. Yoon, W. K. Park, Y. Jung, M. Kwon, W. S. Yang and J.-W. Kang, *Sep. Sci. Technol.*, 2016, **51**, 2958–2969.

37 Y. Gong, C. Qin, W. He, Z. Qiao, G. Zhang, R. Chen, Y. Gao, L. Xiao and S. Jia, *RSC Adv.*, 2017, **7**, 53362–53372.

38 W. He, C. Qin, Z. Qiao, G. Zhang, L. Xiao and S. Jia, *Carbon*, 2016, **109**, 264–268.

39 V. Le Borgne, H. Bazi, T. Hayashi, Y. A. Kim, M. Endo and M. A. El Khakani, *Carbon*, 2014, **77**, 857–867.

40 H. Feng, R. Cheng, X. Zhao, X. Duan and J. Li, *Nat. Commun.*, 2013, **4**, 1539.

41 Z. Bo, X. Shuai, S. Mao, H. Yang, J. Qian, J. Chen, J. Yan and K. Cen, *Sci. Rep.*, 2014, **4**, 4684.

42 J. Chen, B. Yao, C. Li and G. Shi, *Carbon*, 2013, **64**, 225–229.

43 Q. Zhang, H. Zheng, Z. Geng, S. Jiang, J. Ge, K. Fan, S. Duan, Y. Chen, X. Wang and Y. Luo, *J. Am. Chem. Soc.*, 2013, **135**, 12468–12474.

44 Y. Gao, C. Qin, Z. Qiao, B. Wang, W. Li, G. Zhang, R. Chen, L. Xiao and S. Jia, *Carbon*, 2015, **93**, 843–850.

45 Y. Gong, D. Li, Q. Fu and C. Pan, *Prog. Nat. Sci.*, 2015, **25**, 379–385.

46 A. Navaee and A. Salimi, *RSC Adv.*, 2015, **5**, 59874–59880.

47 Y. Qi, M. Yang, W. Xu, S. He and Y. Men, *J. Colloid Interface Sci.*, 2017, **486**, 84–96.

48 J. N. Tiwari, K. Mahesh, N. H. Le, K. C. Kemp, R. Timilsina, R. N. Tiwari and K. S. Kim, *Carbon*, 2013, **56**, 173–182.

49 M. Heidarizad and S. S. Şengör, *J. Mol. Liq.*, 2016, **224**, 607–617.

50 Y. Wang, Y. Xie, Y. Zhang, S. Tang, C. Guo, J. Wu and R. Lau, *Chem. Eng. J.*, 2016, **114**, 258–267.

51 S. Bai, X. Shen, X. Zhong, Y. Liu, G. Zhu, X. Xu and K. Chen, *Carbon*, 2012, **50**, 2337–2346.

52 R. Yu, Y. Shi, D. Yang, Y. Liu, J. Qu and Z. Z. Yu, *ACS Appl. Mater. Interfaces*, 2017, **9**, 21809–21819.

53 H. Yuan, E. Debroye, G. Caliandro, K. P. Janssen, J. van Loon, C. E. Kirschhock, J. A. Martens, J. Hofkens and M. B. Roeffaers, *ACS Omega*, 2016, **1**, 148–159.

54 M. J. Li, C. M. Liu, H. B. Cao and Y. Zhang, *Adv. Mater. Res.*, 2013, **716**, 127–131.

55 N. Pan, L. Li, J. Ding, S. Li, R. Wang, Y. Jin, X. Wang and C. Xia, *J. Hazard. Mater.*, 2016, **309**, 107–115.

56 J. P. Gallivan and D. A. Dougherty, *J. Am. Chem. Soc.*, 2000, **122**, 870–874.

57 M. Kousha, E. Daneshvar, M. S. Sohrabi, M. Jokar and A. Bhatnagar, *Chem. Eng. J.*, 2012, **192**, 67–76.

58 E. R. Garcia, R. L. Medina, M. M. Lozano, I. Hernandez Perez, M. J. Valero and A. M. M. Franco, *Materials*, 2014, **7**, 8037–8057.